Measured Performance of a 50-m2 Kite on a Trawler

Morgan Behrel, ENSTA Bretagne, Brest/France, morgan.behrel@ensta-bretagne.org
Nedeleg Bigi, ENSTA Bretagne, Brest/France, nedeleg.bigi@ensta-bretagne.org
Kostia Roncin, ENSTA Bretagne, Brest/France, kostia.roncin@ensta-bretagne.fr
Damien Grelon, MERINOV, Grande Rivière/Canada, damien.grelon@merinov.ca
Frederic Montel, ENSTA Bretagne, Brest/France, frederic.montel@ensta-bretagne.fr
Alain Nême, ENSTA Bretagne, Brest/France, alain.neme@ensta-bretagne.fr
Jean-Baptiste Leroux, ENSTA Bretagne, Brest/France, jean-baptiste.leroux@ensta-bretagne.fr
Christian Jochum, ENSTA Bretagne, Brest/France, christian.jochum@ensta-bretagne.fr
Yves Parlier, beyond the sea®, La Teste de Buch/France, yves.parlier@beyond-the-sea.com

Abstract

This paper describes an onboard measurement campaign held in Grande-Rivière, Gaspésie, province of Québec, Canada, in October 2015, involving a 13-meter trawler equipped with a 50-square-meter kite. The aim of the campaign was the assessment of the boat performances when kite is used. To achieve this objective, in addition to the kite control system, a set of sensors has been installed. Thus data was recorded, as boat velocity, force generated by kite, fuel consumption, boat attitude, torque and rotational speed of propeller shaft, rudder angle and wind velocity. First, maneuverability tests have been done without kite, following as far as possible the ITTC guidelines. This aimed to get data to benchmark a maneuvering model based on the parametrical models of Yoshimura and Ma. A good agreement between the experimental data and the simulation is observed. Second, runs with kite in static flight have been done, with around 12 knots of true wind speed. The data post processing has allowed to estimate a lift to drag ratio around 6 of the kite and the tethers. This is consistent with other experimental data published.

Nomenclature

Roman Letter

$\underline{\underline{A}}$	Generalized Added Mass Matrix
B	Max beam on waterline
$\underline{\underline{C}}$	Centripetal matrix (6x6)
C_B	Hull block coefficient
C_L	Lift coefficient of the kite
C_{WP}	Water plane area coefficient
d	Draft
d_M	Draft at mid-ship
D_P	Propeller Diameter
Fi	Component of the kite force along the i-axis into the reference frame subscripted
J	Propeller advance ratio
K_Q	Torque coefficient
K_T	Thrust coefficient
L	Distance between the bow on waterline and rudder shaft
L/D	Lift to drag ratio of the kite
$\underline{\underline{M}}$	Generalized rigid body mass matrix (6x6)
n	Rotational speed
Q	Torque
r	Yaw turning rate
R_T	Total resistance
t	Thrust deduction factor
T	Propeller thrust
u	Surge velocity
$\underline{U}$	Velocity vector (3x1)
$\underline{V}$	Generalized velocity vector (6x1)
V_a	Kite apparent wind speed
V_{WR}	Relative Wind speed at kite altitude
$\underline{V}_{WR}$	Relative Wind velocity vector at kite altitude
$\underline{V}_{WT}$	True Wind velocity vector
v	Sway velocity
w	Wake fraction

Greek Letter

β	Drift angle
β_{WR}	Relative wind angle at kite altitude (relative to ship axis)
γ	Flow rectification factor
η	Efficiency

ρ	Fluid density	P	Propeller
ρ_a	Air density during experiments	R	Rudder
ρ_w	Water density	WT	True Wind
$\underline{\Omega}$	Turning rate vector (3x1)	SSB	Shaft stuffing box
Subscript		S	Ship
APP	Appendage	w	water
H	Hull	WR	Relative Wind
K	Kite		

Reference Frames

$\Re_0$ is the earth fixed coordinate system, using the North East Down (NED) convention.

$\Re_C$ is the current coordinate system. It is in rectilinear motion in $\Re_0$ with a constant velocity vector equal to the on-site current.

$\Re_S$ is the ship coordinate axis system, rigidly fixed to the ship. It is defined with the Z-axis pointing down, the X-axis pointing forward, and the Y-axis pointing to starboard. The origin of reference frame is at mid-ship, in the intersection between the center plane of the boat and the water plane.

$\Re_{LF}$ is the low frequency ship coordinate axis system. It is defined with the Z-axis always vertical pointing down, the X-axis into the boat center plane, always horizontal, pointing forward, and the Y-axis pointing to starboard.

$\Re_{WR}$ is the relative wind coordinate axis system at kite altitude. It is the result of a rotation about axis Z_{LF} of angle (β_{WR} - π) applied to frame $\Re_{LF}$.

$\Re_K$ is the body reference frame attached to the kite, assumed as a rigid body.

1.Introduction

The use of kite to extract energy from wind is not a new idea, as it can be seen in *Loyd (1980)*. However, the current growing shortage of fossil resources and the emergence of new ecological regulations force us to reconsider options more renewable, and the use of kite is one of them. The various ways to extract energy with kites have been properly summarize in *Fagiano and Milanese (2012)* and *Cherubini et al. (2015)* give a good oversight of technologies. The current research project, undertaken by the company beyond-the-sea®, and managed in partnership with ENSTA Bretagne, aims to develop kite as auxiliary propulsion system for ships.

For this purpose, numerical models have been developed at ENSTA Bretagne, and so forces generated by kite and associated fuel savings can be predicted by *Leloup et al. (2016)*. Other models are also under development, in particular a parametrical maneuvering model to simulate the interaction between the kite and the ship. All these tools need to be validated, and experimental comparison is one of the best way to do it. In this context, a sea trial and measurement campaign has been set up in partnership with a Canadian fishing vessel and the Merinov institute. This campaign held in Grande-Rivière, Gaspésie, Province of Québec, Canada in October 2015. The fishing vessel was a 13-meter trawler usually used for fishing shrimp on the Gulf of St. Lawrence. All specifications will be given in the first part. A set of winches and sensors has been installed on board, to control the 50-square-meter kite, and measure the induced effects. All the experimental set up will be describe in the second part.
Previously, ships towed by kite have been studied for the purpose of prediction of fuel savings. Naaijen and Koster in *Naaijen et al. (2006)* and *Leloup et al. (2016)* have predicted fuel saving using an average kite towing force over a closed kite loop trajectory. Nevertheless, since the kite behavior is highly dynamic, the dynamic ship motions induced by a kite must be studied. Indeed, a kite could seriously affect the maneuvering characteristics of a ship. Consequently, a dedicated tool has been developed for the beyond-the-sea® project by *Bigi et al. (2016)*. This tool consists in solving the Newton's first law of motion of the multi-body system, ship, tether and kite. In the aim of being

adapted to a wide range of ship, the maneuvering model used in this tool is based on the parametric nonlinear model of *Yoshimura and Masumoto (2012)*. This parametric maneuvering model has been identified with 12 different ships, from a fishing vessel of 26 m long to a container ship of 230 m long. Since the Steven Paul is only 13 m long a validation of the model with experimental data obtained during the campaign is necessary. These data come from maneuverability tests without kite that were carried out, following as far as possible the International Towing Tank Conference (ITTC) recommended procedures 7.5-04-02-01. The validation of the maneuvering model is presented and discussed with one turning circle of both directions (to starboard and to port).

In the last part, a method for computing lift and drag ratio and lift coefficient of the kite is presented. This method is specifically adapted to the available data which were acquired. Indeed, due to a lack of some information about kite orientation during flight and about the wind along the altitude, strong assumptions and estimations have to be done, leading to results which must be interpreted with caution. However, the obtained lift to drag ratios and lift coefficients make sense with other experimental works like *Dadd (2012)* one.

2. General presentation of experimental set up

2.1. Characteristic of the kite

The kite used during trials had an area of 50 m^2 (34 $m^2$of projected area), with an inflatable leading edge, and 9 inflatable battens (see Fig.1). With this architecture, the kite has his own shape without any aerodynamic load, so launching and recovering procedure are easier. The mass of the deflated kite with bridles is 21 kg. Four 60-m-tethers link the kite to the boat. The two main ones, so-called front tethers, are linked to the bridle system attached on the leading edge, and resume about 80% of forces generated by kite. Their lengths are constant. The 20% remaining are taken by the back tethers, which are linked to another bridle system attached on the battens. Back tether are used to control kite flight, and for this purpose their lengths can vary. The attachment point of the tethers was located just ahead the forward bulkhead of the wheelhouse, as it can be seen in Fig.5. The mass of the 4 tethers is 2 kg.

Fig. 1: Kite used during measurement. C-shape with inflatable leading edge and battens, 50 m², 23 kg (deflated, with bridles and tethers).

For launching and recovering procedure, all tethers are wound on the same winch. For control purpose, each back tethers goes through a special pulley system, whose length is adjustable using electric winches. Each one is powered with 24 V DC, and can deliver 700W of nominal power. Optical encoders are fixed on each motor to ensure a feedback to the control system. The latter is running Windows 7, and the software controlling motors operates in LabVIEW (National Instruments). This one allows two mode of control: automatic and manual. The automatic one maintains the kite on a specified stationary position, using a small Inertial Measurement Unit (IMU) attached on the kite to get a feedback on kite position and orientation. The IMU uses a wireless connection to send data to the control system. This autopilot can only ensure static flight, which means the kite can only fly on the wind window edge. It has been developed by engineers of beyond-the-sea®, but this paper does not aim to give more details about it. The manual mode allows the operator to control directly the motor, using two joysticks. The first joystick acts on the differential length between the two back tethers, and so on the direction of the kite. The second joystick is used to trim simultaneously the

length of the two back tethers, that means adjust the global angle of incidence of the kite. The kite control system is fully independent of the data acquisition system that will be described later.

2.2. Characteristics of the vessel

The trials were conducted on a 13-m fishing vessel, called Steven Paul, Table I, Figs.2 and 5, used to fish shrimp with trawl on Saint Laurence gulf during summer season. The Steven Paul, like the majority of the fishing vessels of the area, is equipped with lateral stabilizers to reduce roll motion, and so, improve working quality of the crew. Internal structure modifications were carried out to allow the use of a towing kite, especially reinforcing the foredeck on which kite tethers were attached.

Table I: General characteristics of the fishing vessel Steven Paul

Length Overall	13.39	m
Length of waterline (trials loading conditions)	12.89	m
Length between perpendiculars	12.28	m
Beam of the hull	5.61	m
Displacement (trials loading conditions)	64	T
Displacement (full load)	90	T
Maximum Draft (trials loading conditions)	2.66	m
Draft (full load)	3.23	m
Motorization	Caterpillar 3408 - 480hp	-
Propulsion	Ducted Propeller	-
Crew for fishing operations	Captain with 2 seamen	-

Fig. 2: Steven Paul

Fig. 3: On-board picture of the kite in static flight during one of the starboard run

A Caterpillar 480 horse power engine ensures the propulsion of the vessel (model Marine 3408). At full power (during trawling operation or maximum transit speed), the fuel consumption is about 80 liters per hour. A reduction gear, with a transmission ratio of 1:4.48 transfers power to the propeller (Fig.4). The latter is a 4 blades ducted propeller, with diameter of 1.26 meter. A grid is protecting propeller from unidentified floating objects or from the fishing ropes in case of problem during trawling operation. The characteristics of the propeller are given in Table II. The rudder is a flat plate (Fig.4), 1.45 meter high, for 0.84 meter long, driven by a hydraulic actuator.

Table II: Propeller characteristics of the fishing vessel Steven Paul

Propeller Diameter	1.26	m
Number of blades	4	-
Pitch Ratio	1.015	-
Blade Area Ratio	0.55	-

Fig. 4: Steven Paul propeller and rudder

2.3. Data acquisition system

The whole data acquisition system is based on a National Instruments CompactRIO platform. It consists of 3 main parts: a set of I/O modules depending on sensor technology, a Field-Programmable Gate Array (FPGA, NI CRIO-9114) and a Real-Time processor (NI CRIO-9024). All I/O modules are connected to the FPGA, and the very accurate clock of the FPGA ensures a good synchronization between the channels, and precise acquisition frequencies. The Real-Time processor logs all data coming from sensor through the FPGA on a non-volatile memory. The following table gives the details of I/O modules which have been used for this campaign. All acquisition programs have been developed with LabVIEW. Raw data were all stored in a single file, using a National Instruments proprietary format (TDMS file). These files were then converted into MATLAB® format files, and all calibration procedures and data processing were done using this software.

Table III: Summary of National Instrument I/O module used for data acquisition

Module	Description	Total number of channels
2 x NI 9870	Serial Port	8
1 x NI 9411	Digital Input	6
2 x NI 9237	Bridge Analog Input	8

3. Sensors

3.1. Kinematics of the vessel

To measure motions and velocities of the boat, an IMU coupled with a GPS was set up (Xsens MTi-G-700). This Unit includes a microprocessor able to realize data fusion, based on an extended Kalman filter providing roll and pitch information. Manufacturer ensures dynamic error for roll and pitch under 1° with a 1σ RMS error of 0.1°. The acquisition frequencies of the Xsens were 50Hz for inertial sensors (gyroscope and accelerometer), 20 Hz for roll and pitch, and 5Hz for all data regarding GPS technology (position and velocity). The Xsens was directly linked to a serial port of the CompactRIO. It was fixed in the wheelhouse, just behind the forward bulkhead, a few centimeters behind the attachment point of the kite, located ahead this bulkhead.

To avoid complex and uncertain calibration procedure of magnetometers, it has been decided to use an existing on board sensor to get yaw information, based on dual antenna GPS, instead of yaw information provided by the magnetometers of the Xsens. The sensor was a Si-Tex Vector Pro, with 1σ RMS error under 0.3°. This sensor, providing the true heading of the boat regardless the boat velocity, is used by the onboard autopilot. Therefore, a serial link was done between the autopilot and the CompactRIO to recover this information. The maximum update rate of the Si-Tex Vector Pro is up to 20Hz, according to the manufacturer. However, because the information goes through the

autopilot before reaching the data acquisition system, the final update rate was 1Hz. This could not be changed during the campaign.

3.2. Engine and rudder system

A double flowmeter had been installed previously on the engine, to measure the fuel feed and fuel return, and so provide fuel consumption (Maretron M2RSP-2R-E8). This sensor is connected to the on board NMEA 2000 network. A conversion device on the NMEA2000 network provides a serial output with NMEA183 protocol. This output was connected to another serial port of the CompactRIO, and so the fuel flow was logged at 1Hz. A device measuring the torque on the propeller shaft, developed by the company UpDaq, had also been installed previously on board. A strain gauge had been stuck on the shaft and is linked to an amplifier, sending data wirelessly to a receiver in the wheelhouse. The later was connected to the acquisition system through a serial link. The torque on the shaft was logged at 20Hz. The measurement of rotational speed of the shaft propeller was carried out thank to a binary sensor, going from 0 V to 5 V each time the magnet stuck on the shaft passes nearby the sensor. The sensor was directly linked to the Digital Input module (NI 9411) of the CompactRIO system. The rotational speed of the shaft was logged at 20Hz. A rudder angle sensor was part of the autopilot system to provide feedback. This information had been retrieved using the existing serial link presented part 3.1, with a resolution of 1°, and a frequency of 1Hz.

3.3. Kite

To get force on tethers, load cells had been used during trial. A three dimension load cell (Michigan Scientific TR3D-4K) had been rigidly fixed on the foredeck, just in front the forward bulkhead of the wheelhouse. The location in $\Re_S$ reference frame is (3.1m, 0m, 1.7m). This load cell has a full scale load of 17,800 N for each axis, with a safe overload of 300%. The selection process of the load cell range was done using simulation tools developed by *Leloup et al. (2016)*. During measurement phases, i.e. excluding launching and recovering procedures, the front tethers of the kite were directly connected to this load cell (no idler pulleys). So, this sensor provided information of force vector generated by the kite, expressed into the load cell axis system in a first time, and into the boat axis system after post processing (the position and orientation of the load cell implantation had been of course carefully measured). Knowing the length of tethers, and considering tethers are straight, the position of the kite in the flight window can be recovered. The non-linearity error specified by manufacturer is under 0.5% of full scale, and hysteresis and repeatability errors are under 0.05% of full scale each. It was impossible on the boat to carry out a complete calibration of measurement chain, so sensibilities provided by manufacturer had been used. The global error of the chain including amplifier error and load cell implantation measurement error, was still unknown, however it seems reasonable to expect a global error under 1% of the full scale load.

Measurement of forces in back tethers was different due to the variable length of these tethers to ensure kite control. Two one dimension load cell (Futek LCM200) were installed into the pulleys system, and each one measured twice the load passing through each back tether. These load cells have a full scale load of 4,500N, with a specified non-linearity error under 0.5% of full scale, a hysteresis error under 0.5% of full scale and repeatability error under 0.1% of full scale. Here again, full calibration procedure was impossible to carry out on board, so sensibilities given on calibration certificate of each load cell has been used. The fact that measurement of back tether forces were done into a pulley circuit adds incertitude in measurement. The used pulleys were high-class ones with ball bearing design (Harken Carbo 57 mm), so it is sensible to expect limited effects, although no test in laboratory was carried out. To take all these unknown errors into account the global error in measurement has been raised to 2% of full scale. Each load cells and each axis of the 3D load cell were connected to one of the bridge analogical input of the CompactRIO system. The frequency of acquisition of all channels was 1 kHz.

3.4. Wind

Measurement of relative wind was done using an ultrasonic anemometer (LCJ Capteurs CV7) fixed at 9.01 m from the water line, and 0.3m aft the mid-ship. The update rate of the sensor is 2 Hz, with a direction resolution of 1° and wind module resolution of 0.05 m/s. The sensor was linked to one of the serial port of the CompactRIO platform, using NMEA183 protocol. The roll and pitch motion of the boat were small (maximum ±1°), with averaged periods of 2.9s for pitch and 10s for roll. These motions have induced a maximum velocity at the anemometer level of 0.2 m/s, and it has been decided to neglect these effects.

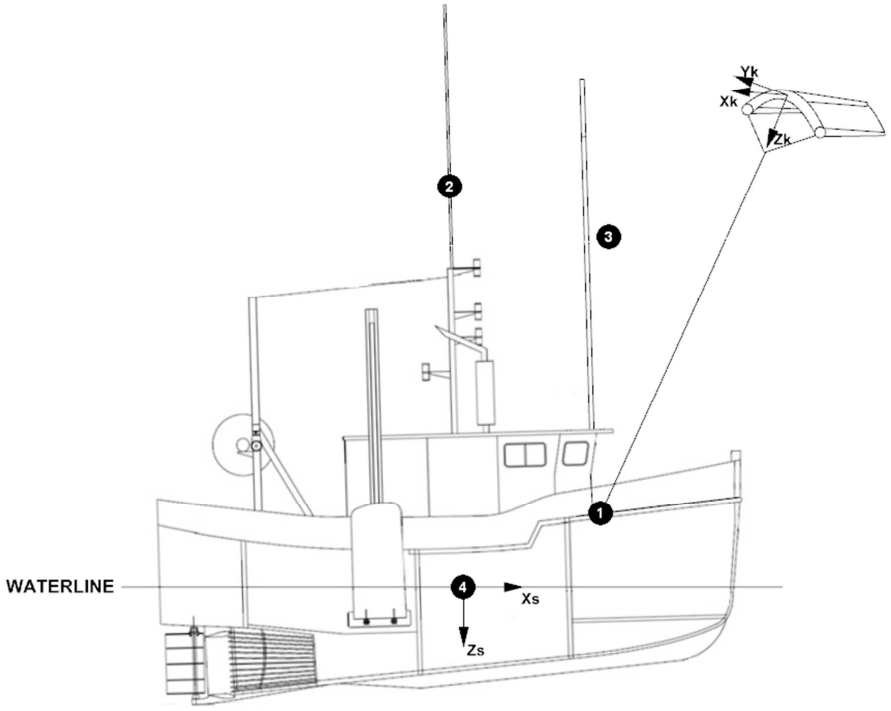

Fig. 5: Side view of the Steven Paul with the waterline as it was during measurements. The marker 1 denotes the kite attachment point and so the position of the 3D load cell described part 3.3. The marker 2 shows the position of the anemometer described part 3.4. The marker 3 notes the launching mast used for launching and recovering procedure. The marker 4 shows the mid-ship of the boat and the origin of the $\Re_s$ reference frame. Kite size and tether length are not true to scale.

4. Comparison of a parametric maneuvering model with experimental data

4.1. Parametric nonlinear maneuvering model

Assuming the ship as a rigid body, the ship equation of motion, in the ship coordinate system $\Re_s$, is written in Eq. (1) as proposed by *Perez (2006)*.

$$(\underline{\underline{M}}_S + \underline{\underline{A}}_S)\dot{\underline{V}}_S + \underline{\underline{C}}_S\underline{V}_S = \underline{F} = \underline{F}_H + \underline{F}_R + \underline{F}_P + \underline{F}_{APP} + \underline{F}_K \quad (1)$$

$\underline{\underline{M}}_S$ is the generalized mass matrix (6x6). $\underline{\underline{A}}_S$ is the generalized added mass matrix (6x6). $\underline{V}_S$ is the generalized ship velocity vector relative to $\Re_C$ expressed in $\Re_S$ at mid-ship. $\underline{V}_S = [u_S \quad v_S \quad w_S \quad p_S \quad q_S \quad r_S]^T$ is the assembly of the linear ship velocity $\underline{U}_S = [u_S \quad v_S \quad w_S]^T$ with the ship angular velocity $\underline{\Omega}_S = [p_S \quad q_S \quad r_S]^T$. $\dot{\underline{V}}_S$ is the generalized velocity time derivative. $\underline{\underline{C}}_S$ is the centripetal matrix (6x6). $\underline{F}$ is the generalized force vector representing the forces acting on the ship. It can be decomposed into the sum of the hull, rudder,

propeller, appendages and kite contributions. In Eq. (8) the subscripts $_H$, $_R$, $_P$, $_{APP}$ and $_K$ denote respectively the hull, the rudder, the propeller, the appendages and the kite. $\underline{F} = \begin{bmatrix} X & Y & Z & L & M & N \end{bmatrix}^T$, where the three first components of F represent the forces and the last three components represent the moments.

Here, the kite is not considered, consequently $\underline{F}_K = \underline{0}$. Moreover, Eq. (1) is reduced to three classical maneuvering degrees of freedom (dof), surge sway and yaw. For instance, X_H is the longitudinal component of the hull force and is expressed by the following Taylor's expansion:

$$X_H = R_T(u_S) + \frac{\rho_w}{2} L\, d_M \left\| \underline{U}_S \right\|^2 \left(X'_{\beta\beta}\beta^2 + X'_{\beta r}\beta\, r' + X'_{rr} r'^2 + X'_{\beta\beta\beta\beta}\beta^4 \right) \tag{2}$$

Yoshimura and Masumoto (2012) provide a parametric formulation of the hull derivatives. Each derivative can be function of the length, width, block coefficient, trim and draft at mid-ship without considering the false-keel. The hull block coefficient denoted by C_B is calculated with the ship length between perpendiculars, the draft at mid-ship and the maximum hull beam. As example, $X'_{\beta\beta}$ is written as follows:

$$X'_{\beta\beta} = 0.185 C_B \frac{B}{L} - 0.18 \tag{3}$$

Here, the rudder model used is the nonlinear model proposed by *Soding (1998)*. On single screw ship a dissymmetry can be noticed between maneuvers with positive and negative turning rate. The presented maneuvering model takes this effect into account by using custom flow rectification factor at the rudder, for each side. Indeed the transverse flow velocity at the rudder in $\Re_S$, denoted by $v_{F,R}^{(S)}$, is expressed as follows:

$$v_{F,R}^{(S)} = -\gamma^{+,-}\left(v_S + x_R r_S \right) \tag{4}$$

Where, x_R is the longitudinal position of the rudder and $\gamma^{+,-}$ is the flow rectification factor. γ^+ is used for positive turning rate and γ^- for negative turning rate.

The thrust deduction fraction can be estimated by the method of Weingart for single-screw ship in Eq. (5), described by *Journée (1976)*. In Eq. (5), C_{WP} denotes the water plane coefficient.

$$t = w\left(1.57 - 2.30\frac{C_B}{C_{WP}} + 1.50 C_B \right) \tag{5}$$

4.2. Resistance and power characteristics of the Steven Paul

The resistance and the power characteristics are identified with the experimental data collected during a power test. For five different quasi-steady states of engine power, the ship velocity over ground, the propeller revolution and the torque on the shaft were measured. In order to obtain the ship velocity with respect to the free surface, the current velocity $\underline{U}_C$ is identified according to the IMO Resolution A.751 (1993) with a turning circle done just before the power test. For each steady state the experimental propeller torque coefficient is identified with the following relationship:

$$K_Q^{\exp} = \eta_{SSB} \frac{\overline{Q}_{SSB}}{\rho_w \overline{n}_P^{\,2} D_P^{\,5}} \tag{6}$$

n_P is the propeller revolution per second; Q_{SSB} is the torque measured on the propeller shaft after the propeller and the shaft stuffing box; D_P denotes the propeller diameter ; η_{SSB} is the shaft stuffing box efficiency; the overbar denotes the time average.

Assuming that the Steven Paul propeller is equivalent to Kaplan 19-A of diameter 1.30 m, of pitch

ratio of 1.015, of blade area ratio of 0.55 and assuming the shaft stuffing box efficiency equals to 0.97, the following equation must be verified for each quasi-steady state of the power test:

$$K_Q^{\exp} = K_Q\left(J = (1-w)\frac{\bar{u}_S}{n_P D_P}\right) \tag{7}$$

The open water torque coefficient K_Q is determined according to the regression model proposed by *Kuiper (1992)*. The wake fraction w is then determined in order to verify Eq. (7). A wake fraction of 0.39 is identified with a Bayesian optimization from *Snoek et al. (2012)*. The left hand side and the right hand side of Eq. (7) are plotted in Fig.6.

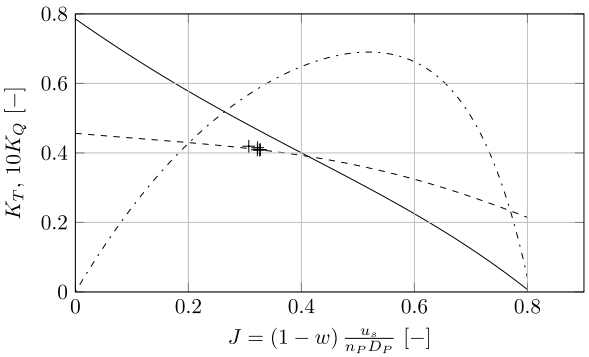

Fig. 6: Comparison between experimental data (denoted by + symbol) and model of K_Q (dashed line) as a function of the propeller advance ratio J. The solid line shows K_T and the dash-dotted line shows the propeller efficiency.

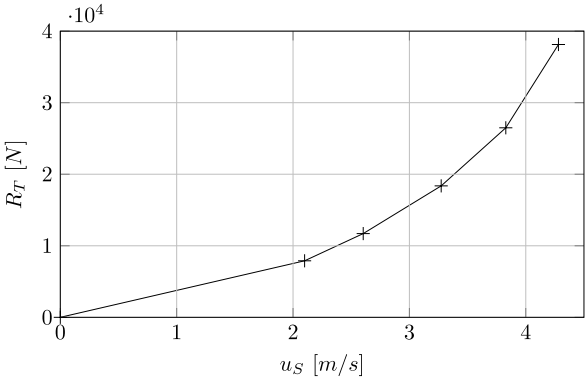

Fig. 7: Total resistance of the Steven Paul calculated with the presented method.

The very high value of wake fraction could be explained by the presence of a protection cage upstream of the propeller. This cage may drastically decrease the mean inflow velocity on the propeller disk area. According to Eq. (5), a thrust deduction factor of 0.34 is obtained. Finally, the total resistance $R_T = \dfrac{(1-t)K_T}{D_P K_Q}\eta_{SSB} Q_{SSB}$ is plotted in Fig.7.

4.3. Validation of the maneuvering model

In order to validate the Steven Paul maneuvering model, one turning circle of each side has been tested. The ship motions during the maneuvers are computed using the experimental rudder angle and the experimental propeller rotational speed as inputs. The two time series at the bottom of Fig.9 represent respectively the experimental rudder angle and the propeller rotational speed. In addition, in Fig.9, ship velocity (surge and sway) and yaw turning rate are plotted. In Fig.8 the computed ship path and the measured ship path are compared. Here, the custom values of the flow rectification factor have been optimized in order to obtain the experimental turning radius, consequently, $\left[\gamma^+ \quad \gamma^-\right] = \left[0.95 \quad 0.61\right]$.

The transient part until $t = 10$ s and the steady part after $t = 10$ s can be distinguished. A good agreement can be noticed for the surge and sway velocity and the yaw turning rate during the steady part of the motion. Regarding the transient part of the turning circle, the decelerating of the simulated surge velocity is lower than the experiments especially on starboard. Moreover, a delay is observable in term of yaw motion in Fig.9, which is confirmed in term of ship path. Despites the observable differences, especially for the transient part, the maneuvering model can be considered as validated, according to the measurements uncertainties and the usual maneuvering validation results available in the literature *Stern et al. (2011)*.

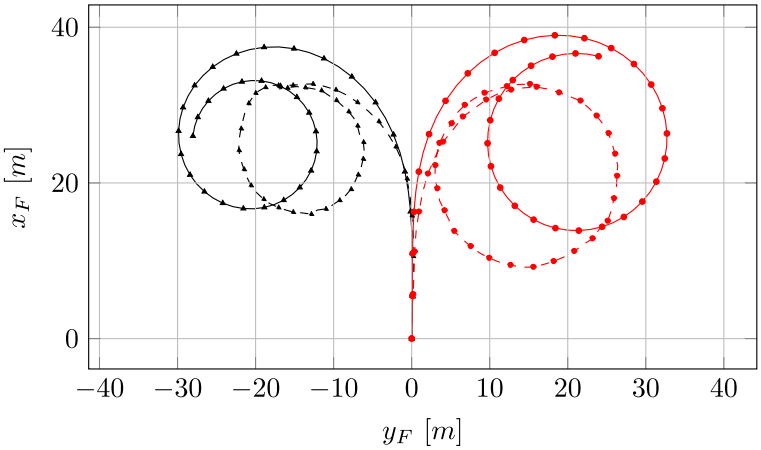

Fig. 8: Ship path during turning circles to portside and to starboard. Dashed and solid lines denote respectively the experimental data and simulated data; triangle and circle marks denote respectively the turning circles to portside and to starboard.

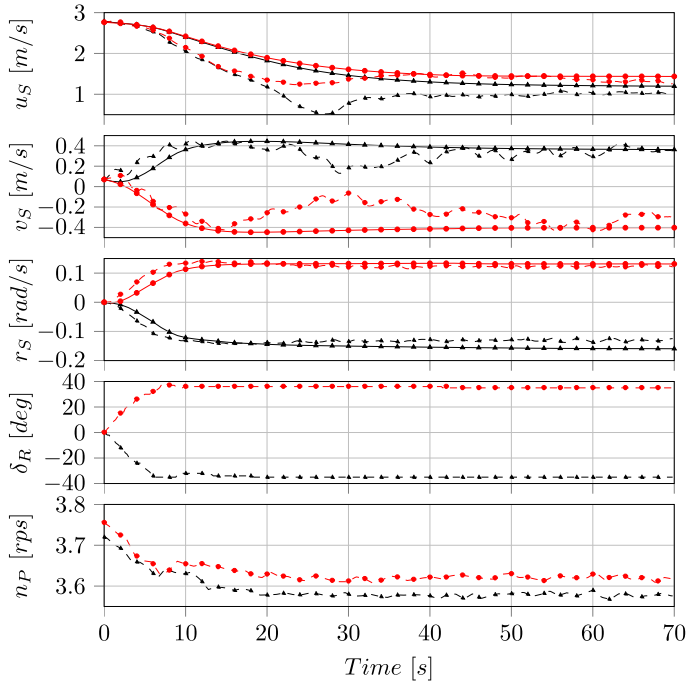

Fig. 9: From the top to the bottom respectively time series of: surge and sway velocity; yaw turning. rate; rudder angle; propeller revolution per second. Dashed and solid lines denote respectively the experimental data and simulated data; triangle and circle marks denote respectively the turning circles to portside and to starboard.

5. Post-processing of kite flight data

During the campaign, due to availability issues with the boat and inoperable weather, only one day of exploitable measurement was able to be achieved. During this day, runs with kite in static flight have been done, with about 12 knots of true wind speed. The aim of the following part is to process data to retrieve lift to drag ratio of the system {kite + tethers}. However, the measurement of the lift to drag ratio is largely affected by the wind intensity and direction at the altitude of the kite (as it will be shown in Eq. (11)), which is an unknown data, as there is no reliable mean to measure it. Indeed only the relative wind over the boat, at 9 m over the sea, is known (see part Fig.5). The absolute wind at the same place can be easily retrieved using speed and heading information, but the absolute wind at other

altitude can only be estimated. Indeed, altitude impacts absolute wind both in strength and direction. With no possibility of getting precise modelling of the twist of the flow along the altitude, it has been decided to neglect the effect of twist, and only take account the 2D shear stress distribution calculated using the Eq. (9), from the ITTC 2011 recommendations. Equations (8) to (10) present the process to go from relative wind velocity and boat velocity measurement to relative wind velocity for any altitude z.

$$\underline{V}_{WT}(Z_0) = \underline{V}_{WR}(Z_0) + \underline{V}_S \tag{8}$$

$$\underline{V}_{WT}(z) = \left(\frac{z}{Z_0}\right)^n \underline{V}_{WT}(Z_0) \tag{9}$$

$$\underline{V}_{WR}(z) = \underline{V}_{WT}(z) - \underline{V}_S \tag{10}$$

Where Z_0 is the altitude measurement (m), z is the altitude above sea level (m) and n is a coefficient which is equal to 1/7 (ITTC 2011). With the relative wind vector defined for any altitude, we can create a new axis system based on it. Hence the Relative Wind reference frame is defined with the X-axis along the relative wind vector at the kite altitude, the Z-axis vertical pointing down and the Y-axis completing the coordinate system to create a direct one. This reference frame is noted with the subscript WR.

Because kite position measurement was done through a 3D load cell rigidly attached to the boat, boat motions affects kite position measurement. This is visible in figure 9 where elevation angle θ of the kite, resulting from the basic transformation of Cartesian position coordinates of the kite into spherical ones, according to boat axis system, evolves in line with the pitch of the boat. To remove these effects, position coordinates of the kite have been expressed into the $\Re_{LF}$ axis system, independent from the boat pitch and roll motion. The transformation matrix is created from the first two Euler angles (roll and pitch) provided by the inertial measurement unit Xsens, according to *Xsens Technologies (2014)*. Result of the transformation is given in Fig.10, showing a few seconds of a starboard run with kite in static flight.

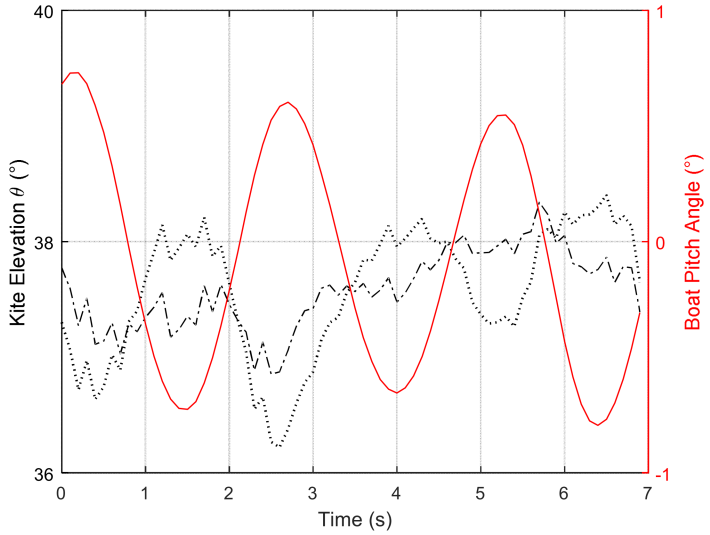

Fig. 10: Expression of kite elevation angle in the $\Re_S$ reference frame (dotted line) and in the $\Re_{LF}$ reference frame (dash-dotted line), during one of the runs with kite in static flight. The first one is in line with the pitch angle of the boat (solid red line) due to the way the measurement of kite position was done.

To process the lift to drag ratio and lift coefficient, the apparent wind on the kite needs to be known. This one is the vectorial difference between the relative wind and the kite velocity in the $\Re_{LF}$

reference frame. For the specific case of static flight, with the ship moving a constant velocity, the kite velocity is theoretically zero in the low frequency ship axis system. However kite in static flight undergoes small but permanent displacement around a middle position, but these displacements are mainly sideslip motion. With the used experimental set up, the yaw orientation of the kite was not measured, so the kite velocity vector cannot be known in the $\Re_K$ reference frame. To deal with this issue, it has been decided to consider the kite in perfect static flight at all times, i.e. the kite velocity in the $\Re_{LF}$ reference frame is taken equal to 0. In other words, the kite is considered as continuously located on the wind window edge as defined by *Leloup et al. (2016)*, and the apparent wind vector is equal to the relative wind vector and is included in the symmetry plane of the kite assumed as a rigid body.

5.1. Lift to drag ratio estimation

From there, it becomes easy to compute lift to drag ratio by expressing kite forces in the $\Re_{WR}$ reference frame. Indeed, the coordinate of the force along X_{WR}-axis is the total drag, and the projection into the (Y_{WR}, Z_{WR}) plane is the lift. The component of force along the Z_{WR}-axis is the sum of the vertical aerodynamic force generated by kite and the weight P of the kite and tethers (equals to 226 N). The latter is then subtracted to the vertical component of force to get only aerodynamic force. Finally the lift to drag ratio is achieved by processing the following equation:

$$L/D = \frac{\sqrt{Fy_{WR}{}^2 + (Fz_{WR} - P)^2}}{Fx_{WR}} \tag{11}$$

5.2. Lift Coefficient Estimation

The previous part has shown the identification of lift and drag component of kite force, from the measured force expressed in the relative wind axis system. From there, and with the same assumptions, lift coefficient can be processed easily using Eq. (12).

$$C_L = \frac{L}{\frac{1}{2} \cdot \rho_a \cdot A_k \cdot V_a{}^2} = \frac{\sqrt{Fy_{WR}{}^2 + (Fz_{WR} - P)^2}}{\frac{1}{2} \cdot \rho_a \cdot A_k \cdot V_{WR}{}^2} \tag{12}$$

A_k is the projected kite area (34 m^2), ρ_a is the density of the air, estimated to 1.22 $kg \cdot m^{-3}$ during the measurement day (air temperature 15°C, atmospheric pressure 1012 hPa, relative humidity 70%), V_a is the kite apparent wind speed, equal to the relative wind speed V_{RW} in case of static flight.

5.3. Results

The Eq. (11) and Eq. (12) have been processed for 3 runs with kite in static flight. Results are presented in Table IV. No kite setting was modified during or between periods, which means the global lengths of back tethers were maintained constant (no change in global angle of incidence of the kite). Only differential variations of tether lengths were done for control purpose, and to keep the kite on a static defined position. The period 2 is shown in Fig.11 and Fig.12. Results are varying a lot, but the averaged lift to drag ratio during the considered period is equal to 6.06, and the averaged lift coefficient is equal to 0.76. This seems consistent with other experimental data published like *Dadd (2012)*. Indeed, for a 3-square-meter kite with an aspect ratio of 4.9, Dadd got a lift coefficient of 0.78 and a lift to drag ratio of 6.07. To estimate drag coefficient and so lift to drag ratio of other kite with other aspect ratio, Dadd uses *Abbott and Von Doenhoff (1959)* formulas, assuming both kite are trimmed to produce same lift coefficient. Applying this method to the kite used for the present study (aspect ratio of 5.5), the expected lift to drag ratio should be 6.36.

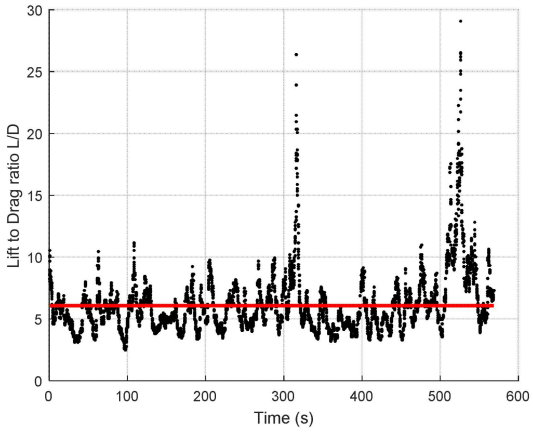

Fig. 11: Lift to drag ratio for each point using Eq. (11) (dotted), during a 569s run with kite in static flight. The solid line is the mean of the lift to drag ratio during the considered period, and is equal to 6.06. The associated standard deviation is 2.45.

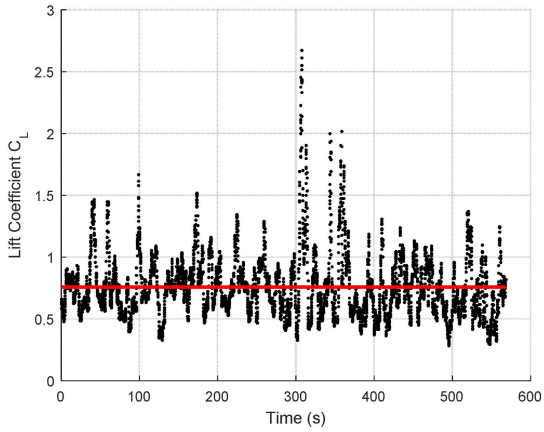

Fig. 12: Lift coefficient for each point using Eq. (12) (dotted), during a 569s run with kite in static flight. The solid line is the mean of the lift coefficient during the considered period (=0.76). The associated standard deviation is 0.26.

Table IV: Compiled results of four periods with kite in static flight

	Dura-tion (s)	Averaged True Wind Speed (m/s)	Averaged True Wind Angle (°)*	Lift to drag ratio L/D		Lift coefficient C_L	
				Mean	Standard deviation	Mean	Standard deviation
Period 1	399	5.7	88	5.9	2.3	0.68	0.21
Period 2	569	6.1	95	6.1	2.5	0.76	0.26
Period 3	209	5.7	304	5.3	1.5	0.59	0.17
*According to boat axis; for example 90° means cross wind, starboard tack							

5.4. Discussion

The averaged results of the 3 periods are close, with also a good agreement with published data, as it has been shown previously. However, the point to point data analysis in Fig.11 and Fig.12 shows extreme values of lift to drag ratio and lift coefficient that are not realistic. This demonstrates the limits of the various assumptions which have been done. One of the most important is probably the consideration of a kite velocity equal to 0 into the $\Re_{LF}$ reference frame, but the straight line assumption could also be a source of incertitude. The decision to disregard the twist wind flow along the altitude due to a lack of data and models could be also detrimental. Thus, a fourth period with kite in static flight has been logged, but it had to be discarded due to inconsistent data. One possible explanation is a significant difference between the wind orientation at the measurement point and the wind orientation at the kite position. This eventuality leads us to consider, for future experimental campaign, a duplication of wind measurement systems. Moreover, the installation of multiple anemometers at various altitudes could be also a good way to improve wind estimation with altitude.
Another goal of the campaign was initially to benchmark the fuel savings prediction tool developed by *Leloup et al. (2016)*, using the flowmeter installed on the engine. However, due to an unexpected unavailability of the boat and unsuitable weather, it has been impossible in only one day to carry out enough measurements alternating runs with kite and then runs without kite with identical weather. Nevertheless, a comparison can be done between power supplied by the kite, and power delivered by the engine to the propeller thanks to the sensors that were installed on-board. For example for the period 2, on the engine side, the average rotation speed of the propeller shaft is 3.4 revolutions per second, and the average torque on the propeller shaft is 1800 Nm. The total power provided by the engine to the propeller is then 38000 W. On the kite side, the average propulsive force generated by the kite during the 569 s is 505 N, the average speed of the boat is 2.4 m/s, so the average power is 1212W. This leads to a kite providing 4.5% of the total power, with only 6.1 m/s of true wind speed, and in static flight condition. Extrapolation of this case to a true wind speed of 12m/s leads then to a

kite providing 17% of the total power required. However this basic estimation needs to be treated very carefully. Indeed this is only one particular case, and does not reflect all operational conditions of the boat. Moreover this estimation does not take into account the effect of kite on the drift for instance. This could induce bigger rudder angles in order to counteract the effects of kite, and so would affect fuel savings. The investigation of these possible issues would be done in a future work using in particular the manoeuvrability model summarily presented and validated in part 4.

6. Conclusion

A full scale kite experimental set up was installed on a13-meter fishing vessel, equipped with a 50-square-meter kite. Boat motions, engine parameters, kite forces, kite positions and wind data were recorded during one day of measurements. First, maneuverability test was carried out to validate a maneuverability modelling of the boat, based on an existing parametrical modelling developed by *Yoshimura and Masumoto (2012)*. A good agreement between experimental data and parametrical modelling is shown. Secondly, multiple runs with kite in static flight were done with various durations, from 3 to 10 minutes. From data which were logged during these runs, a method for estimating lift to drag ratio and lift coefficient has been carried out. This method was computed, and showed results making sense. Thus, a lift to drag ratio about 5.9 and a lift coefficient about 0.7 could be retained (average on the 3 periods). These results are very close of the ones obtained by *Dadd (2012)* even if strong assumptions have been done to get them. These assumptions have been discussed and ameliorations in the experimental set up for future work are under consideration.

Acknowledgements

The authors wish to express their deep appreciation for the full support of the Steven Paul's master-owner, and his great motivation to continuously innovate. The authors are also grateful to the French agency for energy development and control (ADEME) for the funding of this study.

References

ABBOTT, I.H.; VON DOENHOFF, A.E. (1959), *Theory of Wing Sections*, Dover Publ.

BIGI, N.; BEHREL, M.; RONCIN, K.; LEROUX, J.-B.; NEME, A.; JOCHUM, C.; PARLIER, Y. (2016), *Course keeping of ship towed by kite,* 15e Journées de l'Hydrodynamique, Brest

CHERUBINI, A.; PAPINI, A.; VERTECHY, R.; FONTANA, M. (2015), *Airborne wind energy systems: A review of the technologies,* Renewable and Sustainable Energy Reviews 51, pp.1461-1476

DADD, G.M. (2012), *Kite Dynamics for Ship Propulsion*, University of Southampton

FAGIANO, L.; MILANESE, M. (2012), *Airborne wind energy: An overview,* American Control Conf., pp.3132-3143

JOURNÉE, J.M.J. (1976), *Prediction of speed and behaviour of a ship in a seaway,* ISP 23/265, pp.1-24

KUIPER, G. (1992), *The Wageningen propeller series,* MARIN, Wageningen

LELOUP, R.; RONCIN, K.; BEHREL, M.; BLES, G.; LEROUX, J.-B.; JOCHUM, C.; PARLIER, Y. (2016), *A continuous and analytical modeling for kites as auxiliary propulsion devoted to merchant ships , including fuel saving estimation*, Renewable Energy 86, pp.483-496

LOYD, M.L. (1980), *Crosswind kite power (for large-scale wind power production),* J. Energy 4/3, pp.106-111

NAAIJEN, P.; KOSTER, V.; DALLINGA, R.P. (2006), *On the power savings by an auxiliary kite propulsion system*, Int. Shipbuilding Progress 53/4, pp.255-279

PEREZ, T. (2006), *Ship motion control: Course keeping and roll stabilisation using rudder and fins,* Springer

SNOEK, J.; LAROCHELLE, H.; ADAMS, R.P. (2012), *Practical bayesian optimization of machine learning algorithms*, Advances in Neural Information Processing Systems, pp.2951-2959

SÖDING, H. (1998), *Limits of potential theory in rudder flow predictions*, Ship Technology Research 45, pp.141-155

STERN, F.; AGDRUP, K.; KIM, S.; HOCHBAUM, A.; RHEE, K.; QUADVLIEG, F.; PERDON, P.; HINO, T.; GORSKI, J. (2011), *Experience from SIMMAN 2008 - The first workshop on verification and validation of ship maneuvering simulation methods,* J. Ship Research 55, pp.135-147

XSENS TECHNOLOGIES (2014). *MTi User Manual*.

YOSHIMURA, Y.; MASUMOTO, Y. (2012), *Hydrodynamic database and manoeuvring prediction method with medium high-speed merchant ships and fishing vessels*, Int. MARSIM Conf.